Rotational branching ratios and photoelectron angular distributions in resonance enhanced multiphoton ionization of HBr via the F 1Δ2 Rydberg state

Kwanghsi Wang and V. McKoy

Citation: The Journal of Chemical Physics **95**, 7872 (1991); doi: 10.1063/1.461316
View online: http://dx.doi.org/10.1063/1.461316
View Table of Contents: http://scitation.aip.org/content/aip/journal/jcp/95/11?ver=pdfcov
Published by the AIP Publishing

Rotational branching ratios and photoelectron angular distributions in resonance enhanced multiphoton ionization of HBr via the $F\,^1\Delta_2$ Rydberg state

Kwanghsi Wang and V. McKoy
Arthur Amos Noyes Laboratory of Chemical Physics,[a] *California Institute of Technology, Pasadena, California 91125*

(Received 11 July 1991; accepted 27 August 1991)

Results of theoretical studies of rotational ion distributions in the $X\,^2\Pi_{1/2}$ ground state of HBr^+ resulting from $(2+1)$ resonance enhanced multiphoton ionization (REMPI) via the $S(2)$ branch of the $F\,^1\Delta_2$ Rydberg state are reported. These results show a strongly parity-favored ion distribution with about 80% population in the $(-)$ component of the Λ doublet of J^+ rotational levels. The 20% population in the other parity component of the Λ doublet can be seen to be due to odd partial wave contributions to the photoelectron matrix elements which arise primarily from non-atomic-like behavior of the electronic continuum. This, in turn, is due to angular momentum coupling in the photoelectron orbital brought about by the torques of the nonspherical molecular ion potential. We demonstrate that the effect of alignment on these ion distributions, although not large, is important. Photoelectron angular distributions and alignment of the J levels of the HBr^+ ions are also presented. Rotational branching ratios and photoelectron angular distributions resulting from $(2+1')$ REMPI of HBr via several S branches of the $F\,^1\Delta_2$ state are also shown for near-threshold photoelectron energies.

I. INTRODUCTION

Resonance enhanced multiphoton ionization (REMPI) coupled with high-resolution photoelectron spectroscopy has become an important state-selective probe of molecular excited states and their photoionization dynamics.[1-7] Such rotationally resolved REMPI photoelectron spectra have been studied using both the zero-kinetic-energy (ZEKE) photoelectron technique[8,9] and, more generally, time-of-flight measurements[10-14] for a wide range of systems. These studies have clearly demonstrated the rich underlying photoelectron dynamics associated with such state-selective spectra.[6,7] This is particularly true when photoelectron angular distributions are also measured.[11,12] Of specific interest to the present studies are the rotational distributions of HBr^+ ions, deduced by Xie and Zare[15,16] from laser-induced fluorescence (LIF) spectra, resulting from $(2+1)$ REMPI of HBr via the $S(2)$ branch of the $F\,^1\Delta_2$ Rydberg state. LIF studies provide higher resolution than energy-resolved photoelectron studies, allowing, for example, monitoring the populations of individual Λ components of rotational levels of the ion. These spectra[15,16] show a pronounced peak for $\Delta N = N^+ - N' = 0$, with N^+ and N' the rotational quantum numbers of the ionic and intermediate states, respectively, and a strongly $(-)$ parity-favored rotational ion distribution which would result from the expected dominant even partial wave character of the associated photoelectron matrix element. On the basis of selection rules, the 20% population seen in the other $(+)$ parity component would have to arise from odd partial wave contributions to the photoelectron matrix element for ionization of the resonant orbital.[15-17] Recent theoretical studies of these rotational ion distributions[17] showed extremely small populations in the $(+)$ parity component of the Λ doublet, implying that these odd partial wave contributions are entirely negligible here. Autoionization was proposed as a possible underlying mechanism giving rise to the population in the $(+)$ parity components of these ion rotational levels.[17]

In this paper we present results of studies of the rotational ion distributions in the $X\,^2\Pi_{1/2}$ ground state of HBr^+ resulting from $(2+1)$ REMPI via the $S(2)$ branch of the $F\,^1\Delta_2$ Rydberg state. About 20% population is seen in the $(+)$ parity component of the Λ doublet of the ion rotational levels. This agrees well with the results of recent measurements.[15,16] These calculated ion distributions differ significantly from those of earlier studies[17,18] where the $(+)$ parity components were predicted to have extremely small populations. To provide some further insight into the underlying photoelectron dynamics of this REMPI process, an analysis of the partial wave contributions to the rotational ion distributions is given. We also demonstrate that the effect of the alignment in the resonant $F\,^1\Delta_2$ Rydberg state on these rotational ion distributions, although not large, is important. The calculated alignment for individual ion rotational level shows that a significant change in alignment occurs upon ionization. Rotationally resolved photoelectron angular distributions, which clearly reflect the angular momentum composition of the photoelectron continuum, are also shown.

Rotational branching ratios and associated photoelectron angular distributions for $(2+1')$ REMPI of HBr via several S branches of the $F\,^1\Delta_2$ state are also presented for near-threshold or ZEKE-like spectra. The effect of the alignment of the $F\,^1\Delta_2$ state is again illustrated. A number of striking results are found and discussed in detail.

[a] Contribution No. 8472.

 0021-9606/91/237872-08$03.00

II. THEORY AND CALCULATION

A. Differential cross section

The general theory of molecular REMPI processes used in the present studies has been described previously.[19,20] Here we present just a brief outline of some essential features of this approach as it is used to obtain rotational branching ratios and photoelectron angular distributions for HBr^+ ions resulting from $(2+1)$ REMPI of HBr via the $F\,^1\Delta_2$ intermediate state. For linearly polarized light, ionization originating from each of the $(2J_0+1)$ magnetic sublevels of the initial state forms an independent channel. The rotationally resolved differential cross section for ionization out of M_J levels of the resonant intermediate state can be expressed in terms of Legendre polynomials as

$$\frac{d\sigma}{d\Omega} \propto \sum_{\substack{M_J \\ M_{J^+}}} \rho_{M_J M_J} |\Gamma_{M_J M_{J^+}}|^2$$

$$= \frac{\sigma}{4\pi}\left[1+\beta_2 P_2(\cos\theta)+\beta_4 P_4(\cos\theta) + \beta_6 P_6(\cos\theta)+\cdots\right], \quad (1)$$

where σ is the total cross section, β_n the asymmetry parameters, and $P_\ell(\cos\theta)$ the Legendre polynomials. In Eq. (1) $\rho_{M_J M_J}$ is the population of a specific M_J level of the intermediate state created by the two-photon excitation. For the $S(J_0)$ branch of interest here, $\rho_{M_J M_J}$ has the simple form

$$\rho_{M_J M_J} = \Re(J_0+M_J+1)(J_0-M_J+1) \times (J_0+M_J+2)(J_0-M_J+2), \quad (2)$$

where $\Re$ is a normalization constant. In Eq. (2) the M_{J_0} levels of the initial state are assumed to have equal population. This optically induced alignment of the intermediate state may influence the ionic distributions in REMPI processes. An extensive discussion of the role of alignment in the present applications is given in Sec. III. $|\Gamma_{M_J M_{J^+}}|^2$ of Eq. (1) is the probability for photoionization of the M_J level of the intermediate state $|i\rangle$ leading to the M_{J^+} level of the ionic state $|f\rangle$. This ionization probability is proportional to $|\langle f_{\beta,M_{J^+}}|D_{\mu_0}|i_{\alpha,M_J}\rangle|^2$ where D_{μ_0} is the dipole operator in the laboratory frame and $\alpha,\beta = e/f$ designates parity.[21]

The bound-free dipole matrix element can be further expressed in terms of spherical harmonics $Y_{\ell m}(\hat{k})$,[22]

$$\langle f_{\beta,M_{J^+}}|D_{\mu_0}|i_{\alpha,M_J}\rangle = \sum_{\ell m} C_{\ell m} Y_{\ell m}(\hat{k}), \quad (3)$$

with

$$C_{\ell m} = \sqrt{\frac{\pi}{3}}\left[(2J^++1)(2J+1)(2S+1)\right]^{1/2} \times \sum C_{n_+,n'_+} C_{n,n'} F/2\cdot(-1)^{-\Omega+\Sigma}\left[1+(-1)^Q\right] \times \left\{\sum \tilde{I}_{\ell\lambda\mu;\Sigma_e} G\begin{pmatrix} J^+ & J & J_t \\ -\Omega_+ & \Omega & \lambda_t \end{pmatrix}\begin{pmatrix} S_+ & S_e & S \\ \Sigma_+ & \Sigma_e & -\Sigma \end{pmatrix} + \sum \tilde{I}_{\ell\lambda\mu;\Sigma_e}(-1)^p G\begin{pmatrix} J^+ & J & J_t \\ -\Omega_+ & -\Omega & \lambda_t \end{pmatrix}\begin{pmatrix} S_+ & S_e & S \\ \Sigma_+ & \Sigma_e & \Sigma \end{pmatrix}\right\}, \quad (4)$$

$$F = (-1)^{M_J+S_++1/2}(2J_t+1)(2J_r+1) \times \begin{pmatrix} J^+ & J & J_t \\ -M_{J^+} & M_J & m_t \end{pmatrix}\begin{pmatrix} S_e & \ell & J_r \\ -m_e & m & m_r \end{pmatrix}\begin{pmatrix} J_r & 1 & J_t \\ -m_r & \mu_0 & -m_t \end{pmatrix}, \quad (5)$$

$$G = \begin{pmatrix} J_r & 1 & J_t \\ -\lambda_r & \mu & -\lambda_t \end{pmatrix}\begin{pmatrix} S_e & \ell & J_r \\ -\Sigma_e & \lambda & \lambda_r \end{pmatrix}, \quad (6)$$

$$\tilde{I}_{\ell\lambda\mu;\Sigma_e} = \sum_{\Lambda_f\Sigma_f} \langle \Lambda_+ \lambda|\Lambda_f\rangle\langle \Sigma_+ \Sigma_e|\Sigma_f\rangle I_{\ell\lambda\mu}(\Lambda_f\Sigma_f), \quad (7)$$

$$Q = \Delta J + \Delta S + 2S_e + \Delta p + \ell + 1, \quad (8)$$

and

$$p = \begin{cases} 0 & \text{for } e \text{ states} \\ 1 & \text{for } f \text{ states} \end{cases}, \quad (9)$$

where $\Delta J = J^+ - J$, $\Delta S = S_+ - S$, $\Delta p = p_+ - p$. The C_{n_+,n'_+} are expansion coefficients specifying the perturbed rovibronic states which are taken as eigenstates of the Hamiltonian of the intermediate coupling scheme between Hund's cases (a) and (b).[22] In these equations, Ω denotes the total electronic angular momentum about the internuclear axis, Λ the projection of electronic orbital angular momentum along the internuclear axis, S the total spin, Σ its projection along internuclear axis, $S_e = \frac{1}{2}$ the spin of photoelectron, Σ_e its projection along the internuclear axis, J the total angular momentum, and M_J its projection along the laboratory z axis. From Eqs. (4) and (8), the parity selection rule[22-25]

$$\Delta J + \Delta S + 2S_e + \Delta p + \ell = \text{odd} \quad (10)$$

can be deduced for photoionization of the resonant state.

In the single-particle picture, the photoelectron matrix elements of Eq. (7) for photoionization of an orbital ϕ_i in the molecular frame can be written as

$$I_{\ell\lambda\mu} = (-1)^\ell e^{i\eta_\ell}\int dR\, \chi^*_{v_+}(R) r_{fi}^{\ell\lambda\mu}(R)\chi_{v_i}(R), \quad (11)$$

where

$$r_{fi}^{\ell\lambda\mu}(R) = \sum_{\ell'\ell_0}\langle \Psi_{k\ell\ell'}(r,R)Y_{\ell'\lambda}(\hat{r}')|rY_{1\mu}(\hat{r}')| \times \phi_{i\ell_0}(r,R)Y_{\ell_0\pm 2}(\hat{r}')\rangle, \quad (12)$$

with η_ℓ the Coulomb phase shift, and $\Psi_{k\ell\ell'}$ the partial wave component of the photoelectron orbital[26,27] with the momentum k of the ejected electron. Which partial waves ℓ are dominant depends on how ℓ' and ℓ are coupled via the molecular potential. This ℓ coupling in the photoelectron wave function, in turn, influences the ion rotational distribution and associated photoelectron angular distributions.

B. Multiplet-specific wave functions and potentials

There are three dipole-allowed transition channels for photoionization of the 5π orbital of the $F\,^1\Delta_2$ Rydberg state. The corresponding multiplet-specific final state wave functions $|\Lambda_f\Sigma_f\rangle$ are given by

$$\Psi(^1\Pi) = \frac{1}{\sqrt{2}}\left[|(\text{core})4\pi^2_+\, 4\pi_-\, \overline{k\sigma}| - |(\text{core})4\pi^2_+\, \overline{4\pi}_-\, k\sigma|\right], \quad (13a)$$

$$\Psi(^1\Delta) = \frac{1}{\sqrt{2}}\left[|(\text{core})4\pi_+^2\, 4\pi_-\, \overline{k\pi}_+| - |(\text{core})4\pi_+^2\, \overline{4\pi}_-\, k\pi_+|\right], \quad (13b)$$

and

$$\Psi(^1\Phi) = \frac{1}{\sqrt{2}}\left[|(\text{core})4\pi_+^2\, 4\pi_-\, \overline{k\delta}_+| - |(\text{core})4\pi_+^2\, \overline{4\pi}_-\, k\delta_+|\right], \quad (13c)$$

with $(\text{core}) = 1\sigma^2 2\sigma^2 3\sigma^2 4\sigma^2 5\sigma^2 6\sigma^2 7\sigma^2 8\sigma^2 1\pi^4 2\pi^4 3\pi^4 1\delta^4$. Within the frozen-core Hartree–Fock model, the one-particle Schrödinger equation for the photoelectron orbital ϕ_k can be shown to have the form,[26,27]

$$P\left[f + \sum_{i=\text{core}} (2J_i - K_i) + a_n J_n + b_n K_n + \alpha S''_{4\pi} + \beta S'_{4\pi} - \epsilon\right] P|\phi_k\rangle = 0, \quad (14)$$

where J_i and K_i are the Coulomb and exchange operators, respectively, and P is a projection operator which enforces orthogonality of the continuum orbital to the occupied orbitals.[26,27] The operators S'' and S' are defined by

$$S''_\pi \phi_+(\mathbf{r}_1) = \phi_-(\mathbf{r}_1) \int d^3\mathbf{r}_2 [\pi_-(\mathbf{r}_2)]^* \frac{1}{r_{12}} \pi_+(\mathbf{r}_2), \quad (15)$$

and

$$S'_\pi \phi_+(\mathbf{r}_1) = \pi_+(\mathbf{r}_1) \int d^3\mathbf{r}_2 [\pi_-(\mathbf{r}_2)]^* \frac{1}{r_{12}} \phi_-(\mathbf{r}_2). \quad (16)$$

The photoelectron kinetic energy is given by $\epsilon = \frac{1}{2}k^2$. The one-electron operator f in Eq. (14) is

$$f = -\frac{1}{2}\nabla_i^2 - \sum_\alpha \frac{Z_\alpha}{\mathbf{r}_{i\alpha}}, \quad (17)$$

where Z_α is a nuclear charge. Using the wave functions of Eq. (13), the coefficients, α, β, a_n, and b_n associated with the $4\pi_+$ orbital assume values of 0, 0, 2, and -1, respectively. The corresponding values for the $4\pi_-$ level are 0, 0, 1, and 1.

C. Numerical details

For the wave function of the $F\,^1\Delta_2$ $(4\pi \rightarrow 5\pi)$ resonant state, we use the improved virtual orbital (IVO) method[28] in which the core orbitals are taken to be those of the fully relaxed $^2\Pi(4\pi^{-1})$ ion and the (5π) resonant orbital is obtained as an eigenfunction of the static-exchange potential, V_{N-1}, of this core. The orbital basis used in these calculations consists of a [8*s*, 6*p*, 2*d*] contraction of the (15*s*, 12*p*, 5*d*) primitive Cartesian Gaussian basis of Ref. 29 augmented by two *d* functions ($\alpha = 0.55$ and 0.025), two *p* functions ($\alpha = 0.028$ and 0.006), and one *s* function ($\alpha = 0.05$) on the bromine atom. On the hydrogen we use the [3*s*, 1*p*] contraction of a (4*s*, 2*p*) uncontracted Cartesian Gaussian basis of Dunning[30] augmented with two *p* functions ($\alpha = 0.25$ and 0.068). With this basis and choice of wave functions we obtain a total energy of $-2572.630\,92$ a.u. at $R = 2.6729$ a.u. for the $F\,^1\Delta_2$ state.

For the final state we assume a frozen-core Hartree–Fock model in which the core orbitals are taken to be those of the $X\,^2\Pi$ ion and the photoelectron orbital is a solution of the one-electron Schrödinger equation of the form of Eq. (14). To obtain the photoelectron orbitals ϕ_k, we have used an iterative procedure, based on the Schwinger variational principle,[26,27] to solve the Lippmann–Schwinger equation associated with Eq. (14). This procedure begins by approximating the static-exchange potential of the relaxed ionic core by a separable form

$$U_{SE} \approx U_S(\mathbf{r},\mathbf{r}') = \sum_{ij} \langle \mathbf{r}|U|\alpha_i\rangle (U^{-1})_{ij} \langle \alpha_j|U|\mathbf{r}'\rangle, \quad (18)$$

where the matrix U^{-1} is the inverse of the matrix with the elements $(U)_{ij} = \langle \alpha_i|U|\alpha_j\rangle$ and the α's are discrete basis functions such as Cartesian or spherical Gaussian functions. U is twice the static-exchange potential in Eq. (14) with the long-term Coulomb potential removed. The Lippmann–Schwinger equation with this separable potential $U_S(\mathbf{r},\mathbf{r}')$ can be readily solved providing an approximate photoelectron orbital, $\phi_k^{(0)}$. These solutions can be iteratively improved to yield converged solutions to the Lippmann–Schwinger equation containing the full static-exchange potential. In this study, two iterations provided converged solutions of Eq. (14). The basis sets used in the separable expansion of Eq. (18) are listed in Table I.

All matrix elements arising in the solution of the Lippmann–Schwinger equation and elsewhere were evaluated by using single-center expansions about the center of mass. For converged results, the following parameters were used:[26]

(i) maximum partial wave of the photoelectron continuum orbital = 7;

(ii) maximum partial wave expansion of bound orbitals in the direct potential = 60;

(iii) maximum partial wave expansion of the 1σ, 2σ, 3σ, 4σ, 5σ, 6σ, 7σ, 8σ, 1π, 2π, 3π, 4π, 5π, and 1δ bound orbitals in the exchange potential = 30, 30, 25, 25, 20, 20, 15, 15, 30, 25, 20, 15, 15, and 25, respectively;

(iv) maximum partial wave expansion of $1/r_{12}$ in the direct and exchange terms = 60 and 30, respectively;

(v) maximum partial wave expansion of the nuclear potential = 60.

The radial integration grid extended to 64 a.u. and contained 800 points. The integration step sizes ranged from 0.01 to 0.16 up to 16 a.u. and up to 0.16 a.u. beyond this point.

III. RESULTS AND DISCUSSION

A. (2+1) REMPI via the $F\,^1\Delta_2$ Rydberg state

In Fig. 1 we compare our calculated ionic rotational branching ratios resulting from (2 + 1) REMPI of HBr via the $S(2)$ branch of the $F\,^1\Delta_2$ state with the experimental data of Xie and Zare.[16] The photoelectron kinetic energy associated with these spectra is about 2.33 eV. Note that the measured branching ratios shown in Fig. 1 differ from those published previously.[15] Note also that the measured distri-

TABLE I. Basis sets used in the separable potential of Eq. (18).

Symmetry	Center	Type of Gaussian function[a]	Exponents
σ	Br	Cartesian s	8.0, 4.0, 2.0, 1.0, 0.5, 0.25
		z	2.0, 1.0, 0.5, 0.1
	CM	Spherical ($\ell=0$–4)	2.0, 1.0
	H	Cartesian s	1.2, 0.4, 0.1
		z	1.2, 0.4, 0.1
π	Br	Cartesian x	8.0, 4.0, 2.0, 1.0, 0.5, 0.25
		xz	2.0, 1.0, 0.5, 0.25
	CM	Spherical ($\ell=1$–4)	2.0, 1.0
	H	Cartesian x	1.2, 0.4, 0.1
		xz	1.2, 0.4, 0.1
δ	Br	Cartesian xy	16.0, 8.0, 4.0, 2.0, 1.0, 0.5, 0.25, 0.05
	CM	Spherical ($\ell=2$–4)	2.0, 1.0, 0.05
	H	Cartesian xy	1.2, 0.4, 0.1

[a]Cartesian Gaussian basis functions are defined as $\phi^{\alpha,l,m,n,A}(\mathbf{r}) = \mathfrak{N}(X-A_x)^l(y-A_y)^m(z-A_z)^n \exp(-\alpha|\mathbf{r}-\mathbf{A}|^2)$ and spherical Gaussian functions as $\phi^{\alpha,l,m,A}(\mathbf{r}) = \mathfrak{N}|\mathbf{r}-\mathbf{A}|^l \exp(-\alpha|\mathbf{r}-\mathbf{A}|^2) Y_{lm}(\Omega_{\mathbf{r}-\mathbf{A}})$, with $\mathfrak{N}$ the normalization constant.

butions[16] of Fig. 1 have been corrected for the effects of polarization (alignment of the $F\,^1\Delta_2$ state). The agreement between the calculated and measured ion distributions is excellent. As expected from the parity selection rule [Eq. (10)], the (−) parity component (solid bar) of each rotational state is predominantly populated via even partial wave components of the photoelectron matrix element since the 5π orbital of the $F\,^1\Delta_2$ state has an angular composition of 96.57%p, 3.39%d, and 0.03%f character. In addition to the population in the (−) parity components, the (+) parity levels (cross-hatched bar) have about 20% population which agrees well with the measured values.[16] These (+) parity levels are populated via the odd partial wave components of the photoelectron matrix element. Further decomposition shows that about 21.6% of the total ion population arises from s wave contributions, 4.6% from p wave, 51.6% from d wave, 13.5% from f wave, 6.7% from g ($\ell=4$) wave, and 2.0% from higher waves. These distributions reflect the angular momentum composition of the photoelectron matrix element. The partial wave components of the photoelectron matrix element, which are proportional to $|r_{fi}^{\ell\lambda\mu}|^2$(Mb) of Eq. (12), are 2.9305, 0.1873, 1.0551, 0.0631, and 0.0256 for $\ell=0-4$, respectively, in the $k\sigma$ channel, 0.2484, 3.3171, 0.1700, and 0.0322 for $\ell=1-4$, respectively, in the $k\pi$ channel and 4.0879, 1.1459, 1.7574, 0.9466, and 0.3557 for $\ell=2-6$, respectively, in the $k\delta$ channel. These values incorporate a factor of 2.689 ΔE. The main contribution to the population in the (+) parity component of these rotational levels arises from the $5\pi \rightarrow k\delta$ transition. The significant role of the odd partial wave components in these photoelectron matrix elements arises from strong ℓ mixing in the electronic continuum. The photoelectron dynamics of the ionization process is clearly quite non-atomic-like.

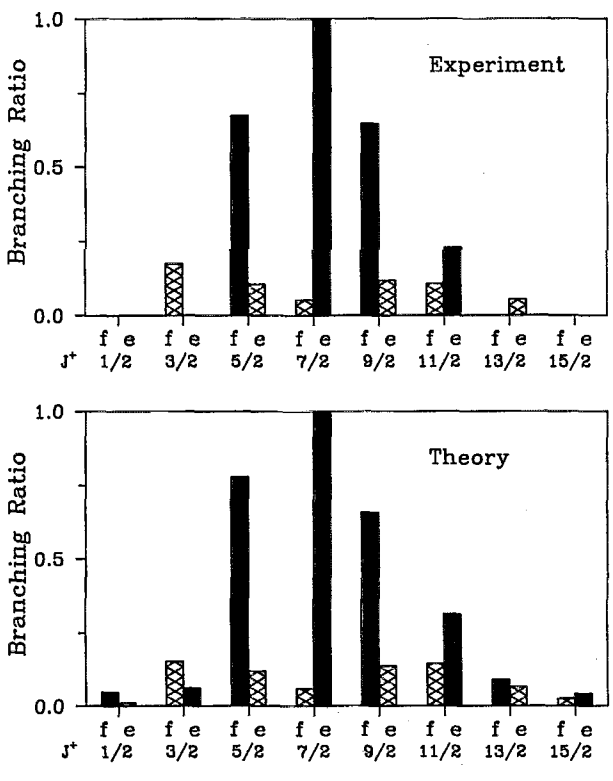

FIG. 1. Experimental and calculated rotational distributions for HBr^+ ($X^2\Pi_{1/2}\,v^+=0$) resulting from (2 + 1) REMPI of HBr via the $S(2)$ branch of the $F\,^1\Delta_2$ Rydberg state. The effect of the alignment of the $F\,^1\Delta_2$ state is included in these calculations. Solid and cross-hatched bars indicate the (−) and (+) parity components of the Λ doublet of a J^+ rotational level, respectively. The photoelectron kinetic energy is about 2.33 eV.

In Fig. 2 we show the calculated rotational ion distributions assuming no alignment in the M_J ($J=4$) levels of the $F\,^1\Delta_2$ state, i.e., all M_J ($J=4$) levels of the $F\,^1\Delta_2$ state are assumed equally populated. The unaligned $F\,^1\Delta_2$ state can be achieved experimentally via two-color REMPI by tuning the angle between polarizations of both lasers to the "magic" angle of 54.7°. The resulting branching ratios show that the population in the (−) parity component of the $J^+ = \frac{9}{2}$ level is larger than that of $J^+ = \frac{5}{2}$. However, the calculated

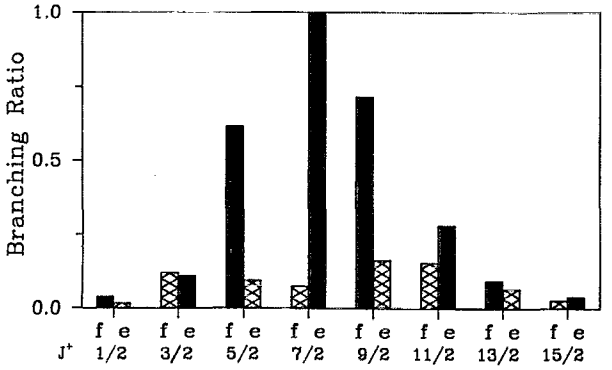

FIG. 2. The same as in Fig. 1 except that the $F\,^1\Delta_2$ state is assumed unaligned in the calculation.

and measured branching ratios of Fig. 1 show that the population in the (−) parity component of the $J^+ = \frac{5}{2}$ level is, in fact, larger than that of $J^+ = \frac{9}{2}$. These results serve to illustrate the subtle role that alignment can play in rotational ion distributions in REMPI of molecular systems. Furthermore, Fig. 3 shows the alignment of M_J levels of the J rotational level of the $F\,^1\Delta_2$ Rydberg state induced by the two-photon excitation [evaluated from Eq. (2)], while Fig. 4 shows the alignment predicted to occur for the different J^+ levels of HBr^+. These populations have been normalized to that of the most intense M_J or M_{J+} level. These results show that a significant change in alignment occurs upon ionization (cf. Figs. 3 and 4). This, in turn, reflects the molecular behavior of the process. The alignment is seen to be significantly different for the $J^+ = \frac{5}{2}, \frac{7}{2}$, and $\frac{9}{2}$ levels. This is particularly so for the $J^+ = \frac{5}{2}$ and $\frac{7}{2}$ levels.

To make a comparison with the calculated results of Ref. 17 we have also obtained the ion rotational branching ratios for $(2+1')$ REMPI via the $S(2)$ branch of the $X \rightarrow F$ transition of HBr at a photoelectron kinetic energy of 1.39 eV, which was assumed there.[17] Figure 5 shows our ion rota-

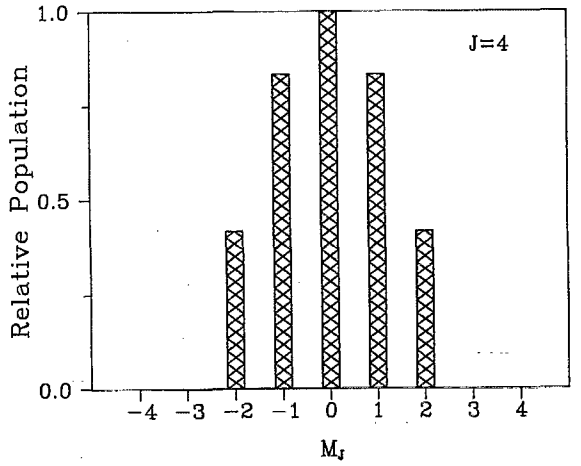

FIG. 3. Relative (aligned) population of the M_J levels ($J=4$) of the $F\,^1\Delta_2$ Rydberg state resulting from $(2+1)$ REMPI via the $S(2)$ branch. Only the (+) parity component of the Λ doublet is populated. The highest intensity has been normalized to unity.

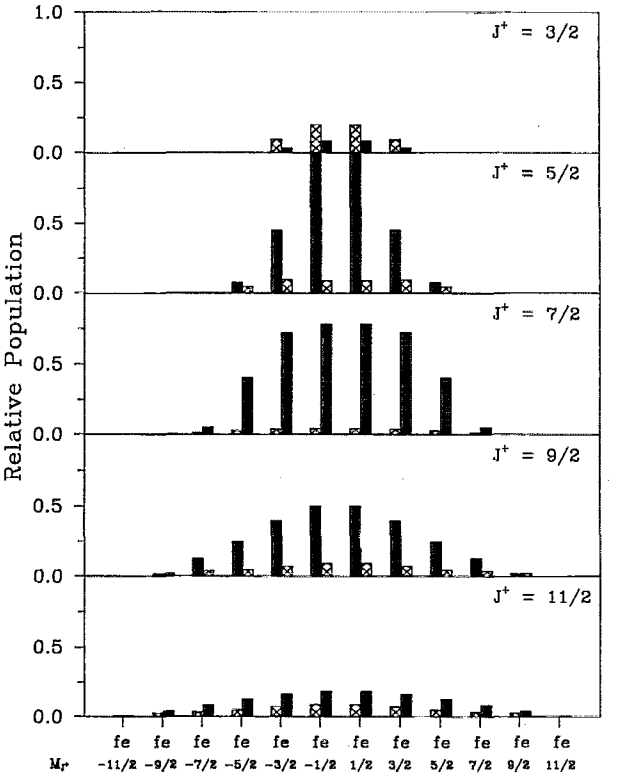

FIG. 4. Relative (aligned) population of M_{J+} levels of J^+ rotational levels corresponding to the calculated ion distributions of Fig. 1. The most intense M_{J+} level is normalized to unity. Other notations are the same as in Fig. 1.

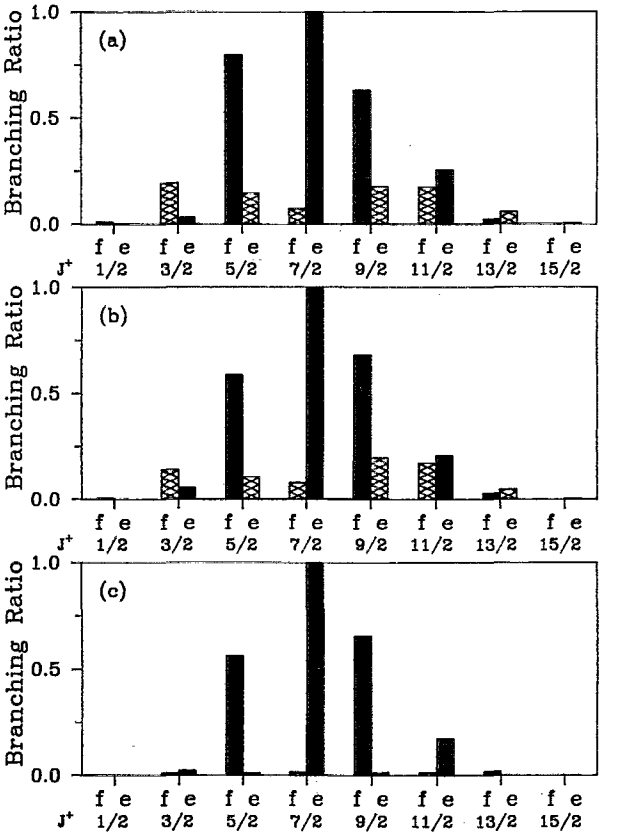

FIG. 5. Rotational ion distributions resulting from $(2+1')$ REMPI via the $S(2)$ branch with (a) and without (b) alignment of the $F\,^1\Delta_2$ Rydberg state. The results of Ref. 17 are shown in (c). The photoelectron kinetic energy is 1.39 eV.

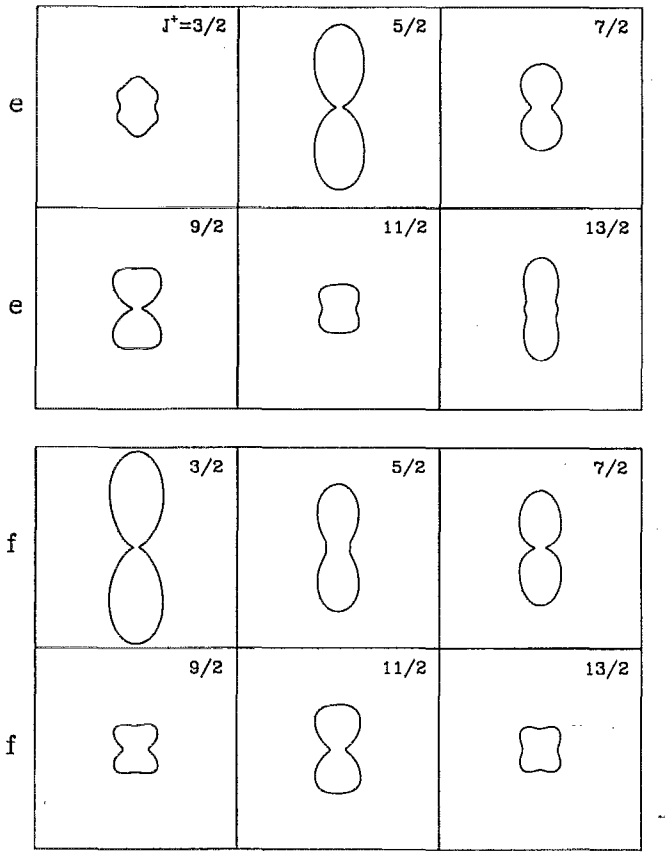

FIG. 6. Calculated photoelectron angular distributions for the rotational levels of Fig. 1. The polarization direction is vertical ($\theta = 0$).

tional distributions calculated with [Fig. 5(a)] and without [Fig. 5(b)] alignment in the $F^1\Delta_2$ state along with the results of Ref. 17 [Fig. 5(c)] where an unaligned state was assumed. The most significant difference between these results is seen in the population of the (+) parity components of the J^+ levels which is negligible in the results of Ref. 17 and is seen to be about 20% in the present calculations. A comparison of the photoelectron matrix elements $|r_{fi}^{\mathcal{A}\mu}|^2$(Mb) (with the factor 2.689 ΔE incorporated) with those of Ref. 17 (in parentheses) is as follows: 0.981 (0.697), 0.094 (0.100), 0.425 (0.444), and 0.066 (0.000) for $\ell = 0 - 3$, respectively, in the $k\sigma$ channel, 0.186 (0.079), 0.729 (0.530), and 0.185 (0.009) for $\ell = 1 - 3$, respectively, in the $k\pi$ channel, and 0.694 (1.250) and 0.280 (0.005) for $\ell = 2 - 3$, respectively, in the $k\delta$ channel. Clearly, the negligible population of the (+) parity component of the J^+ levels predicted in Ref. 17 is due to the low values calculated for the odd partial wave components of the photoelectron matrix element for the $k\pi$ and $k\delta$ channels. Note also that when we neglect alignment in the resonant level, our calculated populations for the (−) parity components of the J^+ levels agree well with those of Ref. 17.

Figure 6 shows the photoelectron angular distributions for the ion rotational levels of Fig. 1. No experimental data is available for these rotationally resolved photoelectron angular distributions. Terms up to β_6 are included in the calculation of these distributions. Note that the photoelectron angular distributions are plotted assuming $\beta_0 = 1$. To examine the underlying angular momentum composition of these photoelectron angular distributions, we show the partial wave contributions to the population of each parity level (e/f) of the J^+ states in Fig. 7. Note that the scales in the different frames in Fig. 7 are different. As expected from the parity selection rule, either even or odd partial waves contribute to the photoelectron angular distribution of each parity component as shown in Figs. 6 and 7. Again we conclude that s and d waves are responsible for the (−) parity component and odd waves, especially $\ell = 3$, are responsible for the other component.

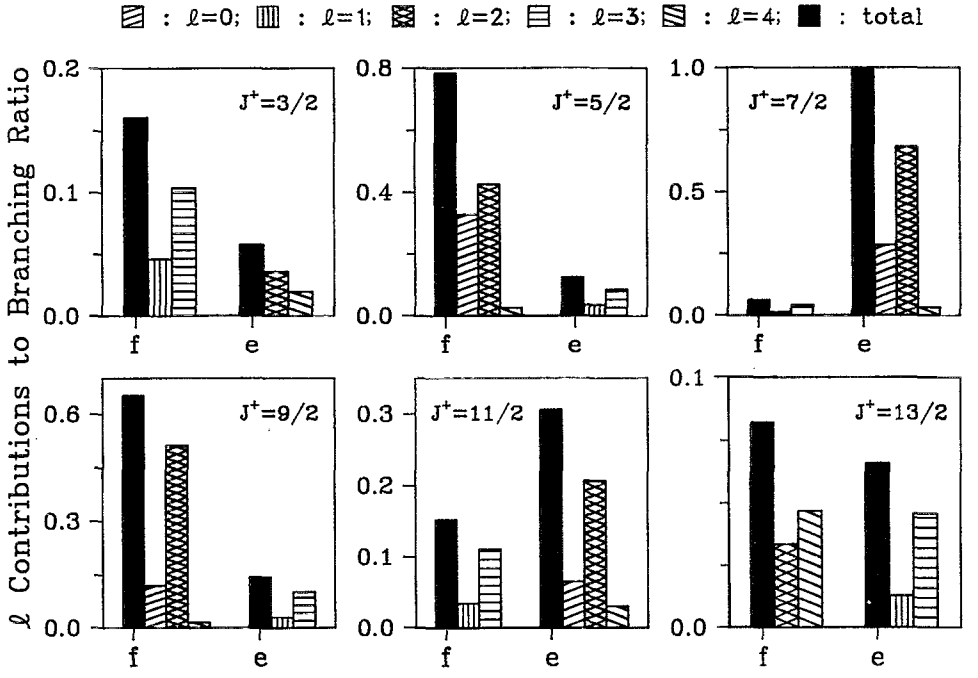

FIG. 7. Partial wave contributions to the rotational ion distributions of Fig. 1. See the text for an explanation.

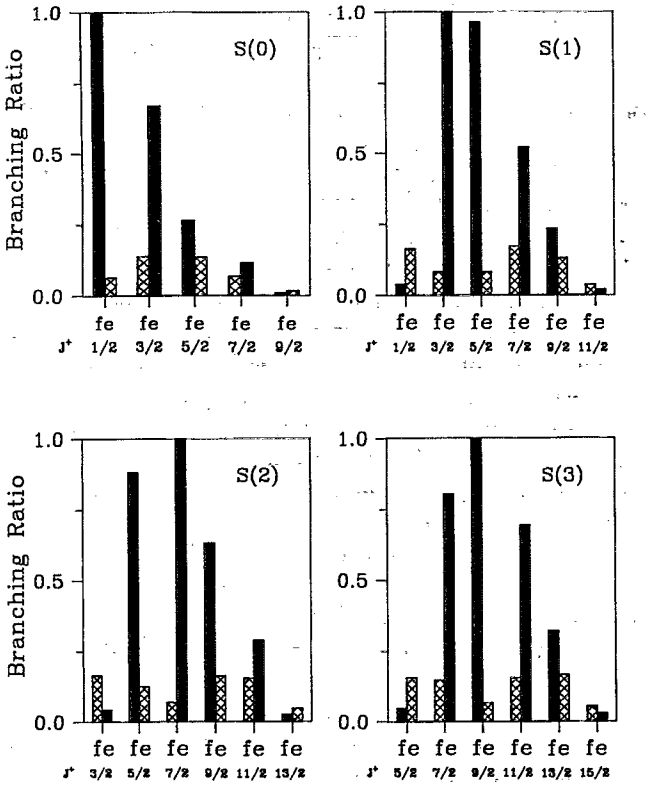

FIG. 8. Calculated rotational branching ratios resulting from $(2+1')$ REMPI of HBr via the $S(n)$, $n=0-3$, rotational branches of the $F\,^1\Delta_2$ intermediate state. The kinetic energy of the photoelectron is 50 meV. Other notations are the same as in Fig. 1.

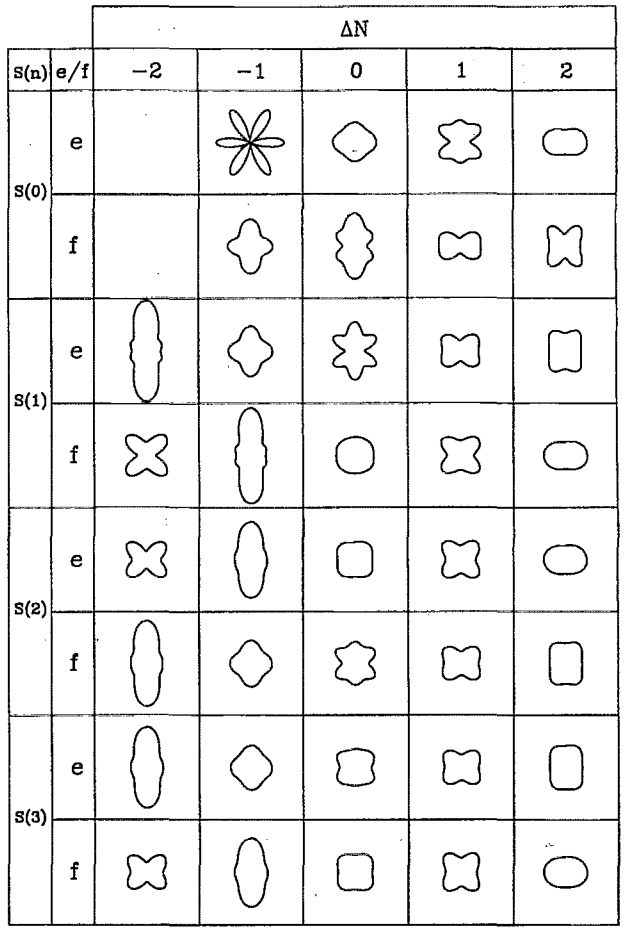

FIG. 9. Calculated photoelectron angular distributions corresponding to the rotational ion distributions of Fig. 8. Asymmetry parameters up to β_6 are evaluated. $\Delta N = N^+ - N' = J^+ + \frac{1}{2} - J$ with $N' = J = n + 2$ for the $S(n)$, $n=0-3$, branches. The polarization direction is vertical $(\theta = 0)$.

B. ZEKE spectra via the $F\,^1\Delta_2$ state

Recently, ionic rotational branching ratios resulting from $(2+1')$ REMPI via the $S(0)$ branch of the $F\,^1\Delta_2$ state of HCl have been measured at near-threshold photoelectron energies.[31] We now look at similar ZEKE spectra of HBr to see how analogous these may be to those of HCl. In Fig. 8 we show calculated ionic rotational branching ratios for $(2+1')$ REMPI of HBr via the $S(n)$, $n=0$, 1, 2 and 3, branches of the $F\,^1\Delta_2$ intermediate state at a photoelectron kinetic energy of 50 meV. Some important features of these spectra include: (i) the $(-)$ parity components (solid bar) of these rotational states of HBr^+ are dominant and are populated by waves of even symmetry; (ii) about 20% of the ion population is still expected in the $(+)$ parity component (cross-hatched bar); (iii) the most intense transitions for the $S(0)$ and $S(1)$ branches are for $\Delta N = N^+ - N' = -1$ peaks. The shift of the most intense transition from $\Delta N = 0$ to $\Delta N = -1$ at low J rotational level is due to the alignment induced by the two-photon excitation; (iv) the ZEKE spectra for the $S(2)$ branch is similar to the rotational distribution of the one-color experiment shown in Fig. 1 indicating that the ion rotational distribution is only slightly dependent on photoelectron kinetic energy; and (v) the total ionic rotational branching ratios (sum of e and f levels) of the $S(0)$ branch are similar to those of HCl.[31]

Figure 9 shows the photoelectron angular distributions corresponding to the ion rotational distributions of Fig. 8. Again, based on the parity selection rule of Eq. (10), only even or odd partial waves contribute to each photoelectron angular distribution of a specific parity component of an ion rotational level. *Contributions from higher ℓ partial waves are very evident in these low photoelectron energy spectra.* Figure 10 shows calculated ionic rotational branching ratios and corresponding photoelectron angular distributions for the $S(16)$ branch of the $F\,^1\Delta_2$ Rydberg state where the high J limit has been reached. The rotational branching ratios are similar to those of the unaligned $F\,^1\Delta_2$ state shown in Fig. 2. The photoelectron angular distributions of the $(+)$ or $(-)$ parity components of the J^+ levels of Fig. 9 are obviously approaching the high J limit behavior of Fig. 10. Similar behavior is also seen in the rotational branching ratios.

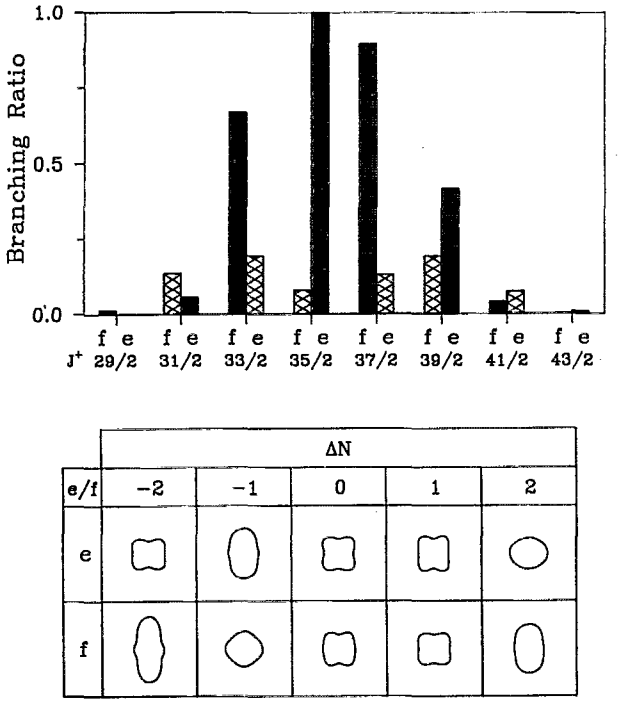

FIG. 10. Calculated rotational branching ratios and associated photoelectron angular distributions for the $(2+1')$ REMPI of HBr via the $S(16)$ branch of the $F\,^1\Delta_2$ state. Other notations are the same as in Figs. 8 and 9.

ACKNOWLEDGMENTS

This work was supported by grants from the National Science Foundation, Air Force Office of Scientific Research, and the Office of Health and Environmental Research of the U.S. Department of Energy. We acknowledge use of resources of the JPL/Caltech CRAY X-MP/18 Supercomputer. We also thank Dr. Jinchun Xie and Professor Richard Zare for kindly making their experimental data available to us prior to publication.

[1] R. N. Compton and J. C. Miller, in *Laser Applications in Physical Chemistry*, edited by D. K. Evans (Dekker, New York, 1988), Sec. 4.
[2] J. W. Hudgens, in *Advances in Multiphoton Processes and Spectroscopy*, edited by S. H. Lin (World Scientific, Singapore, 1988), Vol. 4.
[3] P. M. Dehmer, J. L. Dehmer, and S. T. Pratt, Comments At. Mol. Phys. **19**, 205 (1987).
[4] W. A. Chupka, J. Chem. Phys. **87**, 1488 (1987).
[5] P. M. Johnson and C. E. Otis, Annu. Rev. Phys. Chem. **32**, 139 (1981).
[6] C. Y. Ng, in *Techniques of Chemistry, Vol. 20, Techniques for the Study of Ion–Molecule Reactions*, edited by J. M. Farrar and W. H. Saunders (Wiley, New York, 1988), pp. 417–488.
[7] T. M. Orlando, B. Yang, and S. L. Anderson, J. Chem. Phys. **90**, 1577 (1989).
[8] K. Müller-Dethlefs, M. Sander, and E. W. Schlag, Chem. Phys. Lett. **112**, 291 (1984); M. Sander, L. A. Chewter, K. Müller-Dethlefs, and E. W. Schlag, Phys. Rev. A **36**, 4543 (1987).
[9] M. Braunstein, V. McKoy, S. N. Dixit, R. G. Tonkyn, and M. G. White, J. Chem. Phys. **93**, 5345 (1990).
[10] W. G. Wilson, K. S. Viswanathan, E. Sekreta, and J. P. Reilly, J. Phys. Chem. **88**, 672 (1984); K. S. Viswanathan, E. Sekreta, E. R. Davidson, and J. P. Reilly, *ibid.* **90**, 5078 (1986); K. S. Viswanathan, E. Sekreta, and J. P. Reilly, *ibid.* **90**, 5658 (1986).
[11] S. W. Allendorf, D. J. Leahy, D. C. Jacobs, and R. N. Zare, J. Chem. Phys. **91**, 2216 (1989).
[12] E. F. McCormack, S. T. Pratt, J. L. Dehmer, and P. M. Dehmer, J. Chem. Phys. **92**, 4734 (1990).
[13] M. A. O'Halloran, S. T. Pratt, P. M. Dehmer, and J. L. Dehmer, J. Chem. Phys. **87**, 3288 (1987); M. A. O'Halloran, P. M. Dehmer, S. T. Pratt, J. L. Dehmer, and F. S. Tomkins, J. Chem. Phys. **90**, 930 (1989).
[14] S. T. Pratt, P. M. Dehmer, and J. L. Dehmer, J. Chem. Phys. **92**, 262 (1990).
[15] J. Xie and R. N. Zare, Chem. Phys. Lett. **159**, 399 (1989).
[16] J. Xie and R. N. Zare (private communication).
[17] H. Lefebvre-Brion, Chem. Phys. Lett. **171**, 377 (1990). Note that these rotational ion distributions were calculated at a photoelectron kinetic energy of 1.39 eV which is about 1 eV smaller than that of the experiment of Ref. 15.
[18] Our calculated ion rotational distributions show about the same populations for these (+) parity components both at the actual photoelectron energy (2.33 eV) of the experiments of Refs. 15 and 16 and the photoelectron energy of 1.39 eV assumed in the studies of Ref. 17.
[19] S. N. Dixit and V. McKoy, J. Chem. Phys. **82**, 3546 (1985).
[20] H. Rudolph, S. N. Dixit, V. McKoy, and W. M. Huo, J. Chem. Phys. **88**, 637 (1988).
[21] J. M. Brown, J. T. Hougen, K.-P. Huber, J. W. C. Johns, I. Kopp, H. Lefebvre-Brion, A. J. Merer, D. A. Ramsay, J. Rostas, and R. N. Zare, J. Mol. Spectrosc. **55**, 500 (1975).
[22] K. Wang and V. McKoy, J. Chem. Phys. **95**, 4977 (1991).
[23] J. Xie and R. N. Zare, J. Chem. Phys. **93**, 3033 (1990).
[24] S. N. Dixit and V. McKoy, Chem. Phys. Lett. **128**, 49 (1986).
[25] G. Raseev and N. Cherepkov, Phys. Rev. A **42**, 3948 (1990).
[26] R. R. Lucchese, G. Raseev, and V. McKoy, Phys. Rev. A **25**, 2572 (1982).
[27] R. R. Lucchese, K. Takatsuka, and V. McKoy, Phys. Rep. **131**, 147 (1986).
[28] W. J. Hunt and W. A. Goddard, Chem. Phys. Lett. **3**, 414 (1969).
[29] P. Guillermo Del Conde, P. S. Bagus, and C. W. Bauschlicher, Jr., Theoret. Chim. Acta (Berl.) **45**, 121 (1977).
[30] T. H. Dunning, Jr., J. Chem. Phys. **53**, 2823 (1970); **55**, 3958 (1971).
[31] K. S. Haber, Y. Jiang, G. Bryant, H. Lefebvre-Brion, and E. R. Grant, Phys. Rev. A (in press).